J. Fluid Mech. (1972), *vol.* 55, *part* 2, *pp.* 271–287
Printed in Great Britain

Thermal convection in a horizontal fluid layer with uniform volumetric energy sources

By F. A. KULACKI

Department of Mechanical Engineering, The Ohio State University

AND R. J. GOLDSTEIN

Department of Mechanical Engineering, University of Minnesota

(Received 24 February 1972)

Energy transport at Rayleigh numbers up to 675 times the critical (linear stability theory) value is measured in a layer of dilute electrolyte bounded horizontally by two rigid planes of constant and equal temperature; Joule heating by an alternating current passing horizontally through the layer provides the volumetric energy source. Horizontally averaged temperature profiles are determined optically. Mean temperature distributions are asymmetric at elevated Rayleigh numbers, the energy transport at the upper boundary being more than twice that at the lower boundary. Three regimes of flow are identified and discrete transitions in the energy transport appear to exist when the flow is turbulent. Extrapolation of the data to the conduction value of the Nusselt number yields a critical Rayleigh number which is within $+10{\cdot}7\,\%$ of linear theory values. No subcritical convection is observed when finite amplitude disturbances are introduced into the fluid at a Rayleigh number between the critical values predicted by the linear stability theory and energy theory respectively.

1. Introduction

An initially quiescent fluid layer can be brought to a state of internal convective motion if a sufficient imbalance exists between buoyant forces tending to displace fluid elements and restraining viscous forces. In thermal convection, buoyant forces due to density differences can be produced by differential warming of the fluid at its horizontal boundaries or by warming of the fluid from within. The ratio of the buoyant forces to the viscous forces times the ratio of the heat convected to the heat dissipated by conduction is the characteristic dimensionless group for such systems and is expressed as the Rayleigh number

$$Ra = (g\beta/\alpha\nu)\,\Delta T^* L^{*3},$$

where ΔT^* is the characteristic (destabilizing) temperature difference within the layer and L^* is a characteristic length scale for the layer, generally corresponding to the depth of the portion of the layer in unstable equilibrium. The constants g, β, α and ν are, respectively, the gravitational acceleration, the isobaric coefficient of thermal expansion, the thermal diffusivity and the kinematic viscosity.

Relatively meagre treatment has been given to thermal convection in fluid layers warmed internally by distributed energy sources. In this case, a nonlinear mean temperature or density field in the conduction state preceding the onset of motion is responsible for destabilizing buoyant forces. Thermal convection with internally distributed energy sources has been proposed as a mechanism for the outer regions of stellar interiors by Bethe (1968) and has been considered in connexion with earth-mantle convection by Runcorn (1962), Tozer (1966) and Knopoff (1967).

Several experimental studies on thermal convection in internally heated layers already exist. The works of French (1968), Tritton & Zarraga (1967) and Schwiderski & Schwab (1971) were largely qualitative investigations of the overall nature and character of the fluid motion in the immediate post-stability regime or for moderately elevated Rayleigh numbers. Drawing the results of these studies together, it may be concluded that for $Ra/Ra_c < 80$ (where Ra_c is the linear theory critical Ra) the flow exhibits a cellular planform with downflow in the centre of the cells (counter to that of Bénard convection in liquids). It was found also that the cell orientation and shape reach only a quasi-stationary state for all Ra up to $80Ra_c$, but above this value local turbulent motion was observed.

In the research reported here, thermal convective phenomena in a horizontal fluid layer supporting a uniform (positive) volumetric energy source has been considered. The initial flow instability, the nature of the flow and mean temperature fields in the post-stability regimes, and the heat transport within the layer and at its boundaries have been investigated experimentally. A Mach–Zehnder interferometer was employed to measure the temperature distribution within a layer of dilute aqueous silver nitrate bounded by two rigid isothermal horizontal plane walls maintained at equal temperatures. Joule heating of the electrolyte with a 60 Hz alternating current provided the volumetric energy source.

With the given experimental design, the Rayleigh number is appropriately expressed in terms of the strength of the volumetric energy source; $S = H/\rho C$, where H is the unit volumetric rate of energy production. ΔT^* is set equal to $SL^2/8\alpha$, the maximum temperature difference which would occur in the layer with purely conductive energy transport to the boundaries. Even at large Ra this temperature difference is physically significant since it relates the characteristic parameter of the system to a known, measurable quantity, the power input. The length scale L^* is chosen as $\frac{1}{2}L$, the half-layer thickness, to correspond to this temperature difference (under stable no-flow conditions). Thus, the Rayleigh number is given by

$$Ra = \frac{g\beta}{\alpha\nu}\frac{L^3}{32}\left(\frac{SL^2}{2\alpha}\right).$$

2. Apparatus and instrumentation

The Mach-Zehnder Interferometer of the Heat Transfer Laboratory at the University of Minnesota was used to obtain quantitative information on horizontally averaged temperatures in the layer. A review of the interferometric technique for studying heat transfer in fluids has been given by Goldstein (1968) and its applicability to volume heating studies in liquids was demonstrated by Novotny (1963) and Wilkie & Fisher (1963).

With a liquid as the heat transport medium, an approximation assuming small temperature differences in the fluid relates the horizontally averaged temperature difference in the fluid layer to the interference field by

$$T - T_w = \frac{\epsilon \lambda_0}{X|dn/dT|}, \tag{1}$$

where T_w is the temperature of the horizontal boundaries of the layer, λ_0 is the wavelength of the light source in the interferometer, X is the length of liquid along the light beam and dn/dT is the derivative of the index of refraction of the liquid evaluated at T_w. ϵ, the 'fringe shift', is the optical path length difference in vacuum wavelengths between the two beams of the interferometer relative to that of a light ray passing immediately adjacent to the boundary.

If the interferometer is adjusted to give wedge or 'finite fringes', a series of light and dark bands are formed at the focal plane in the interferometer. When there are no initial temperature differences in the liquid these fringes can be aligned with a vertical reference (e.g. a plumb line). With temperature variation in the liquid, the fringes deviate from the vertical (figure 4, plate 1); the number of fringes crossing the plumb line (i.e. the fringe shift) is proportional to the temperature difference. Equation (1) expresses this relation and is valid at any cross-section in the light beam passing through the fluid. Refraction and edge effects are neglected in (1) but may be corrected on a systematic basis (Goldstein 1968; Novotny 1963). The temperature data given in this paper were corrected for such optical effects (Kulacki 1971).

If the optical components of the interferometer are adjusted so that a single fringe occupies the entire field of view at the focal plane, the 'infinite fringe' adjustment is obtained. The number of interference fringes which form when the fluid is no longer isothermal is also related to the temperature difference by (1). In the present study, the infinite fringe adjustment is better suited to qualitative visualization of the horizontally averaged temperature fields while finite fringes are used for most of the quantitative tests. A single fringe or fringe shift is equivalent to a temperature difference of approximately 0·02 °C in the present study.

The convection chamber comprised a fluid layer of dilute (0·02 molar or less) aqueous silver nitrate solution of varying depths (1·27–6·35 cm) bounded above and below by two copper plates each 25·4 cm square and 2·40 cm thick. The surfaces of the plates in contact with the fluid layer were ground flat to ± 0·00127 cm and were electrically and chemically insulated from the silver nitrate solution by a 0·05 mm film of Mylar. Two side walls had optical windows ground to a $\frac{1}{4}$ wavelength flatness on both sides. The thickness of the optical windows was sufficient to keep distortion due to the maximum hydrostatic loading by the layer of liquid to less than 0·10 wavelength. The other two walls were of Plexiglas and each displaced 1·27 cm from the copper plates. Each of these two Plexiglas walls contained a 0·635 cm thick silver-plated copper flat which served as an electrode

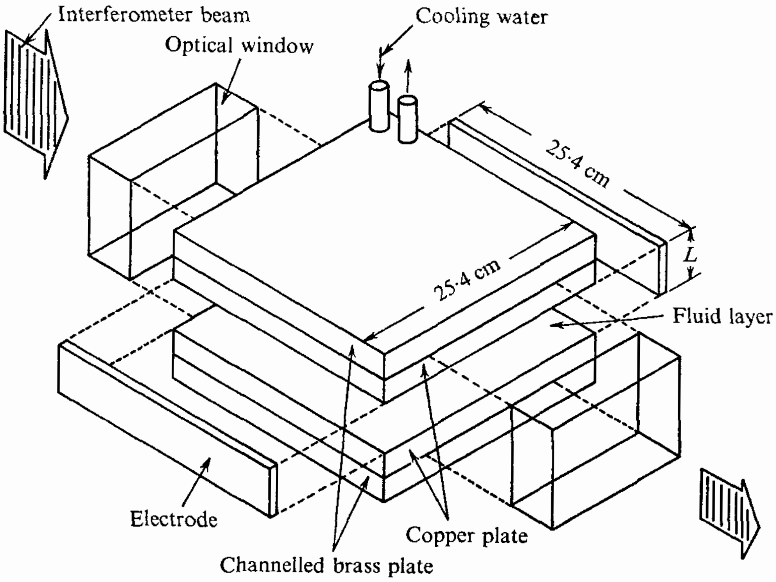

FIGURE 1. Convection chamber. $0.127\ \text{cm} \leqslant L \leqslant 6.352\ \text{cm}$.

for the passage of electric current through the layer. Four 1·27 cm diameter Plexiglas rods were used to separate the upper and lower boundaries of the layer. The lengths of the rods were varied to form layers of different depths. In all the experiments, the horizontal and vertical dimensions of the electrodes were equal to the length and depth of the layer respectively. As the layer depth was varied, electrodes with a vertical dimension equal to the layer depth were inserted into the side walls of the convection chamber. A 5·08 cm thick layer of urethane foam for insulation completely surrounded the chamber during the experiments. A simplified schematic diagram of the convection chamber is given in figure 1.

The temperatures of the upper and lower boundaries of the layer were held constant with thermostatically controlled water circulating through a double-spiral channel brass plate bolted to the back of each copper plate. A gasket of Teflon film 25·4 × 25·4 × 0·00254 cm between the brass and copper prevented leakage. The brass plates were each 2·54 cm thick and were machined with twenty-two channels of 1·27 cm depth. Water was supplied to the channels from a bath with a pumping capacity large enough to allow both the upper and lower channelled plates to be operated in parallel. Temperature control was accurate to within 0·01 °C with regulation of less than 0·04 °C. In practice, small fluctuations in bath temperature produced no measurable changes in the temperatures of the copper plates.

Nine 30-gauge iron–constantan thermocouples were used to monitor the temperatures of each of the copper plates. The thermocouple wells in the plates were drilled to within 0·038 cm of the surface in contact with the test fluid and each thermocouple was electrically insulated from the copper plate by a casing of copper oxide cement in its well. The thermocouples were placed symmetrically about the centre-lines of the plates in rows of three, each 7·72 cm apart. Each thermocouple e.m.f. output was measured with a Honeywell 'Electronik 15' self-balancing potentiometer. Readings could be made to within 0·001 mV (0·019 °C) with an accuracy of 0·002 mV (0·039 °C). Horizontal temperature gradients in the copper plates could not be detected during any of the experiments.

The convection chamber was operated as an electrochemical cell formed by the silver and silver ion in solution at a constant applied voltage. Applied voltages were 35 V or less and the total consumed power was 4·7 W or less in experiments where quantitative temperature data was desired. Electrical power was supplied from line voltage at 60 Hz through a voltage regulator and variable transformer. Power dissipated in the fluid was measured with a wattmeter of $\frac{1}{4}$ % rated accuracy.

Electromagnetic side effects of the applied alternating electric field were found to be negligible. The disturbance of the induced magnetic field in a half-period had a diffusion length of approximately 100 m. The magnetic Reynolds number of the fluid was approximately 10^{-8}.

3. Experimental procedure

Before each experiment, the interferometer was aligned with the test section once the copper plates and fluid layer were in thermal equilibrium at a temperature 0·5 °C below room temperature. The plates were to be held at this temperature during the experiment in an attempt to minimize heat losses. Wedge fringes were then obtained and aligned with a plumb line to ensure that they were vertical. Since the two plates bounding the layer could not be made perfectly parallel, the inclination of the light beam was adjusted to minimize the refractive bending of fringes at both surfaces. During the experiments, refraction and reflexion effects at each boundary produced a zone of 'no information' larger than that due to misalignment.

When the alignment procedure had been completed, a camera was focused on small Plexiglas pins (in some cases a single pin was used) positioned on the lower boundary at the centre of the layer. A photograph of these 'scale pins' served to determine the boundaries of the layer on the interferograms and to relate distance on the interferogram to actual distance in the layer.

After the scale pins had been photographed power was applied to the system. A period of time sufficient for the development of the convective motion was then allowed to elapse before recording an interferogram. Estimates of flow development times for various layer depths were made on the basis of the time required for attainment of a steady one-dimensional temperature distribution in the fluid for pure conduction. In practice, interferograms at smaller plate spacings (low *Ra*) were recorded after a one to one and a half hour period and those at larger plate spacings (high *Ra*) after 2–3 h. In both cases, the allowed flow development times were larger than that required for development of the conduction temperature distribution.

Interferograms were recorded with a 35 mm camera focused at the midplane of the layer at 1 s or at 15 s exposures. Longer time exposures were attempted, but subsequent analysis of these interferograms showed no significant increase in either precision or accuracy of the final energy transport results over that of the short time exposure results. Both local fluctuations and large-scale translations of the fringe field produced wedge fringes of generally poor definition when very long time exposures were used. Thus the interferograms shown in this paper were obtained from 1 and 15 s exposure interferograms and should be regarded as only horizontally averaged (i.e. along the light beam). No distinction is made between data obtained from the interferograms at the two different time exposures.

Temperature gradients at the layer boundaries were computed from direct measurements of fringe gradients corrected for volume heating in the fluid. Very close to the wall, the energy transport was governed largely by one-dimensional heat conduction:

$$d^2T/dz^2 = -S/\alpha, \tag{2}$$

where z is the vertical co-ordinate in the fluid layer. Integration of (2) gives for the temperature gradient at the wall:

$$\left.\frac{dT}{dz}\right|_w = \left.\frac{dT}{dz}\right|_z + \frac{S}{\alpha}(z-z_w). \tag{3}$$

The last term on the right-hand side in (3) is the correction for volume heating. The gradient $[dT/dz]_z$ was computed with a three-point derivative from an interpolating parabola fit through the three fringe shifts closest to the wall. This formulation was less sensitive to small errors in reading fringe shift data near the wall than a simple two-point derivative. The thermal diffusivity in (3) was evaluated at the average wall temperature since the three fringe shift values closest to the wall were typically within 1 mm of the wall.

4. Energy transport results

The striking feature of the convective flow at supercritical Ra is the dominating influence of buoyancy on the warm central region of the layer (see figures 4–8, plates 1–4). With Ra only slightly above the linear theory critical value of 560 (§ 6), the region where the maximum temperature occurs is above the geometric centre of the layer; the mean temperature distribution is asymmetrical and markedly different rates of energy transport occur at the two boundaries of the layer. An average Nusselt number must then be determined for each of the boundaries.

The Nusselt number is defined using the entire layer depth L as the characteristic length dimension and the maximum measured temperature difference $T_{\max} - T_w$ in the layer:

$$Nu = \frac{q_w}{T_{\max} - T_w}\frac{L}{k_f} = \frac{L|dT/dz|_w}{T_{\max} - T_w}. \tag{4}$$

At each Ra, an average Nu for the upper and lower surfaces was computed using a number of temperature profiles over the central region of an interferogram. This was equivalent to averaging the energy transport over the central 5 cm of the layer. The mean value, absolute variation (in the horizontal direction across the light beam) and standard error of the mean value of Nu are given in

L (cm)	Ra	Pr	Nu_1	SE_1	δNu_1	Nu_0	SE_0	δNu_0	n	BF
1·270	196·7	5·966	4·06	0·053	3·82–4·27	4·23	0·169	3·50–4·11	8	1·07
1·270	217·8	6·023	3·78	—	—	3·99	—	—	2	0·98
1·270	258·9	5·966	3·91	0·067	3·78–4·14	3·93	0·075	3·79–4·12	5	0·96
1·270	258·9	5·966	4·37	0·115	3·91–4·88	3·90	0·055	3·67–4·04	9	1·01
1·270	390·9	6·318	4·16	0·021	3·98–4·28	4·05	0·009	3·97–4·08	14	1·07
1·270	390·9	6·318	4·16	0·027	3·99–4·33	4·01	0·008	3·97–4·05	11	1·02
1·270	391·1	5·975	3·93	0·056	3·44–4·37	3·95	0·018	3·85–4·13	14	0·99
1·270	391·1	5·975	4·16	0·042	3·88–4·35	3·93	0·019	3·82–4·02	11	0·99
1·270	391·1	5·975	4·19	0·025	4·02–4·45	3·89	0·022	3·67–4·05	20	0·99
1·270	391·1	5·975	4·10	0·033	3·94–4·28	4·10	0·029	4·00–4·32	10	0·97
1·270	391·1	5·975	4·06	0·046	3·75–4·27	4·06	0·055	3·69–4·29	11	0·97
1·270	404·9	6·312	4·02	0·134	3·50–4·78	3·98	0·019	3·86–4·06	9	1·00
1·429	405·5	5·917	4·08	0·033	3·92–4·30	4·01	0·019	3·89–4·15	14	0·98
1·429	450·2	5·971	4·09	0·019	3·96–4·25	4·00	0·017	3·87–4·14	18	0·98
1·429	497·9	5·972	4·05	0·012	3·99–4·11	4·01	0·012	3·96–4·08	12	0·99
1·429	580·2	5·972	3·98	0·051	3·84–4·13	3·99	0·033	3·87–4·10	6	0·98
1·429	580·5	5·972	3·98	0·053	3·85–4·13	3·95	0·061	3·76–4·08	5	0·98
1·429	620·8	5·855	4·09	0·033	3·87–4·36	3·92	0·026	3·81–4·12	14	0·99
1·429	620·8	5·855	4·09	0·038	3·65–4·44	3·92	0·027	3·80–4·07	19	0·99
1·429	631·2	5·891	4·11	0·016	3·98–4·18	3·92	0·009	3·87–3·98	17	1·03
1·429	671·4	5·871	4·05	0·065	3·48–4·41	3·96	0·027	3·77–4·10	16	1·05
1·565	703·2	6·323	4·17	0·040	3·61–4·43	4·04	0·024	3·92–4·20	18	0·99
1·429	758·0	5·871	4·02	0·035	3·88–4·14	3·98	0·029	3·89–4·08	7	1·05
1·565	802·1	6·345	4·23	0·047	4·03–4·70	3·99	0·047	3·71–4·40	13	0·99
1·565	802·2	6·344	4·22	0·029	4·04–4·38	3·99	0·034	3·80–4·13	14	1·00
1·429	803·5	5·869	4·09	0·041	3·91–4·16	3·94	0·069	3·59–4·36	9	1·01
1·429	818·7	5·891	4·05	0·044	3·92–4·27	3·98	0·079	3·95–4·02	11	1·00
1·429	818·7	5·891	4·14	0·073	3·96–4·38	3·88	0·024	3·77–3·94	6	0·99
1·429	823·7	5·891	4·00	0·013	3·95–4·07	3·96	0·014	3·87–4·02	10	0·99
1·429	823·7	5·890	4·01	0·020	3·88–4·06	3·95	0·015	3·91–4·02	9	0·99
1·429	848·7	5·870	4·09	0·047	3·81–4·22	3·94	0·033	3·67–4·11	19	0·99
1·429	888·4	5·847	4·56	0·038	4·40–4·69	3·97	0·092	3·64–4·30	8	0·98
1·429	888·4	5·857	4·46	0·028	4·26–4·62	3·94	0·053	3·60–4·25	18	0·97
1·565	948·1	6·325	4·11	0·045	3·86–4·57	3·99	0·026	3·90–4·07	13	0·95
1·906	1·104 × 10³	6·053	4·56	0·351	3·99–5·94	3·99	0·053	3·84–4·13	5	1·03
1·906	1·105	6·053	4·14	0·048	3·86–4·45	4·12	0·040	3·95–4·45	13	0·98
1·906	1·542	6·052	5·17	0·039	4·64–5·75	4·30	0·029	4·01–4·53	25	0·96
1·906	1·542	6·052	5·16	0·034	4·90–5·27	4·29	0·032	4·17–4·45	12	0·97
1·906	1·542	6·052	5·19	0·064	4·94–4·75	4·11	0·069	3·84–4·65	12	0·94

TABLE 1. Experimental energy-transport data. $SE = \left(\dfrac{\sum_{i=1}^{n}(Nu_i - Nu)^2}{n(n-1)}\right)^{\frac{1}{2}}$, $\delta Nu = Nu_{\min} - Nu_{\max}$; n = number of profiles.

L(cm)	Ra	Pr	Nu_1	SE_1	δNu_1	Nu_0	SE_0	δNu_0	N	BF
1·906	1·959 × 10^3	6·052	5·22	0·041	5·06–5·33	4·11	0·044	3·97–4·32	7	0·93
1·906	1·959	6·052	5·16	0·061	4·77–5·32	4·21	0·057	3·86–4·45	9	0·92
1·906	2·146	5·762	5·41	0·028	5·06–5·97	4·38	0·039	3·86–4·93	37	1·02
1·906	2·314	5·869	5·33	0·048	4·91–5·95	4·51	0·023	4·43–4·85	24	1·00
1·906	2·642	6·052	6·01	0·028	5·94–6·07	4·35	0·094	4·12–4·53	5	1·09
1·906	2·642	6·052	5·91	0·035	5·60–6·19	4·48	0·061	4·18–5·07	19	1·06
2·539	2·781	5·808	5·89	0·043	5·60–6·39	4·52	0·066	4·13–5·71	26	1·07
2·539	3·121	5·881	6·03	0·093	5·50–6·61	4·53	0·047	4·06–4·95	25	1·07
2·539	3·620	5·807	6·45	0·048	6·05–7·00	4·91	0·046	4·29–5·87	27	1·08
2·539	4·071	6·034	6·23	0·071	5·75–7·36	4·79	0·019	4·62–4·99	21	0·99
2·539	4·783	5·881	7·01	0·112	5·13–9·18	4·99	0·061	4·43–6·03	39	1·12
2·539	5·469	5·859	6·85	0·062	6·29–7·71	4·99	0·055	4·47–6·41	35	1·03
2·539	5·961	5·879	6·97	0·098	6·29–8·19	4·83	0·099	4·14–6·08	26	1·07
2·539	6·552	5·881	7·22	0·069	6·59–8·12	4·93	0·042	4·57–5·26	30	1·07
2·539	6·609	5·880	7·35	0·056	6·99–7·75	4·82	0·037	4·65–5·16	17	1·08
2·539	7·566	6·032	8·32	0·241	6·84–11·6	4·67	0·048	3·97–5·18	27	1·11
2·539	7·593	5·879	7·31	0·202	6·04–9·24	4·94	0·061	4·32–5·43	20	1·06
3·176	8·427	6·086	7·38	0·112	6·71–8·03	4·59	0·065	4·08–4·83	12	1·06
3·176	8·427	6·086	7·85	0·064	7·51–8·12	4·75	0·041	4·54.4·91	11	1·08
3·176	9·629	6·085	7·75	0·065	7·46–7·94	4·78	0·038	4·66–5·01	8	1·06
3·176	1·011 × 10^4	6·039	7·65	0·076	7·10–8·01	5·15	0·068	4·64–5·60	18	1·06
3·176	1·011	6·039	7·58	0·092	7·13–7·76	5·00	0·097	4·70–5·48	8	1·06
3·809	1·241	5·975	9·34	0·057	7·90–8·72	5·00	0·071	4·70–5·92	17	1·18
3·176	1·582	6·086	8·70	0·064	8·44–9·01	5·38	0·080	4·98–5·85	11	1·10
3·176	1·611	6·086	8·78	0·064	8·18–9·09	5·28	0·065	4·89–5·77	18	1·05
3·176	1·845	6·083	9·15	0·109	8·71–9·69	4·73	0·137	4·33–5·67	9	1·05
3·176	1·845	6·083	9·52	0·329	8·77–10·7	4·97	0·136	4·68–5·47	5	1·07
3·809	2·237	5·795	10·02	0·337	8·75–11·8	6·01	0·078	5·83–6·18	8	1·13
3·809	2·909	5·799	9·94	0·173	8·97–11·9	5·40	0·104	4·82–6·04	18	1·07
3·176	3·051	6·048	9·67	0·151	8·37–10·8	5·71	0·061	5·22–6·11	16	1·03
3·176	3·098	5·999	8·63	0·177	7·68–9·19	5·53	0·084	5·04–5·98	9	0·97
3·809	3·632	5·794	10·84	0·093	10·3–11·2	5·63	0·066	5·06–5·91	14	1·18
3·809	4·199	5·793	11·26	0·174	9·47–12·3	5·73	0·079	4·53–6·17	21	1·21
5·079	6·320	5·837	11·58	0·164	10·4–12·5	6·46	0·090	5·81–6·36	15	1·02
5·079	1·025 × 10^5	5·815	12·83	0·116	12·2–13·4	6·26	0·056	6·00–7·10	21	0·98
5·079	1·272	5·815	14·15	0·153	12·0–15·5	6·58	0·071	5·90–7·60	27	1·00
5·079	1·498	5·815	14·79	0·122	13·4–16·1	6·52	0·102	5·14–8·36	35	1·03
5·079	1·673	5·812	14·66	0·115	13·4–15·6	6·29	0·079	5·60–6·90	29	1·04
5·079	2·019	5·812	14·91	0·157	13·5–15·6	6·29	0·054	5·90–6·70	15	1·02
5·079	2·223	5·811	15·48	0·233	13·7–19·0	6·67	0·059	6·30–7·58	25	1·06
5·079	2·487	5·810	16·46	0·174	15·3–17·9	6·97	0·087	6·35–7·46	16	1·05
6·352	2·738	5·853	17·44	1·380	15·5–21·5	6·85	0·046	6·80–6·94	4	1·02
6·352	3·785	5·847	17·43	0·691	15·9–18·7	7·93	0·121	7·59–8·14	4	0·95

TABLE 1. (*Continued*)

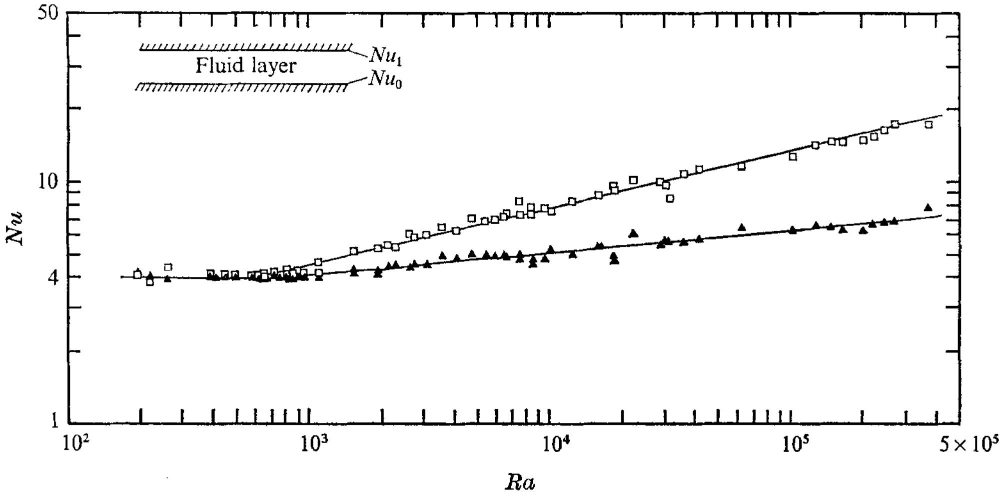

FIGURE 2. Dimensionless energy-transport data and correlations. —□—, $Nu_1 = 0{\cdot}879Ra^{0{\cdot}236}$; —▲—, $Nu_0 = 2{\cdot}111Ra^{0{\cdot}094}$.

table 1. Average values of Nu correlated well with all supercritical Ra, assuming a relation of the form

$$Nu = CRa^m. \tag{5}$$

At the upper boundary

$$\left.\begin{array}{l} Nu_1 = 0{\cdot}879Ra^{0{\cdot}236\pm0{\cdot}003}, \quad 580 \leqslant Ra \leqslant 3{\cdot}78\times10^5, \\ 5{\cdot}76 \leqslant Pr \leqslant 6{\cdot}35, \quad 0{\cdot}05 \leqslant (L/X) \leqslant 0{\cdot}25, \\ r = 0{\cdot}994 \quad \text{from 67 observations,} \end{array}\right\} \tag{6}$$

and at the lower boundary

$$\left.\begin{array}{l} Nu_0 = 2{\cdot}111Ra^{0{\cdot}094\pm0{\cdot}002}, \quad 580 \leqslant Ra \leqslant 3{\cdot}78\times10^5, \quad 5{\cdot}76 \leqslant Pr \leqslant 6{\cdot}35, \\ 0{\cdot}05 \leqslant (L/X) \leqslant 0{\cdot}25, \quad r = 0{\cdot}978 \quad \text{from 67 observations,} \end{array}\right\} \tag{7}$$

where $Pr = \nu/\alpha$ and r is the correlation coefficient. These correlations and the experimental data are summarized in figure 2. No significant reduction in the error sum of squares of the regression of Nu on Ra could be obtained by including either Pr or the layer aspect ratio L/X in the correlation. The fraction of the total energy dissipation removed at the upper boundary of the layer, $Nu_1/(Nu_1+Nu_0)$, is given in figure 3.

The data are almost as well represented (compare coefficients of correlation) by (5), assuming $m = 0{\cdot}25$ and $m = 0{\cdot}10$ for the upper and lower boundary respectively. A least-squares fit of the data in these cases gives for the upper boundary

$$Nu_1 = (0{\cdot}756\pm0{\cdot}005)Ra^{0{\cdot}25} \quad 580 \leqslant Ra \leqslant 3{\cdot}78\times10^5, \quad 5{\cdot}76 \leqslant Pr \leqslant 6{\cdot}35,$$

$$0{\cdot}05 \leqslant (L/X) \leqslant 0{\cdot}25, \quad r = 0{\cdot}990 \quad \text{from 67 observations,}$$

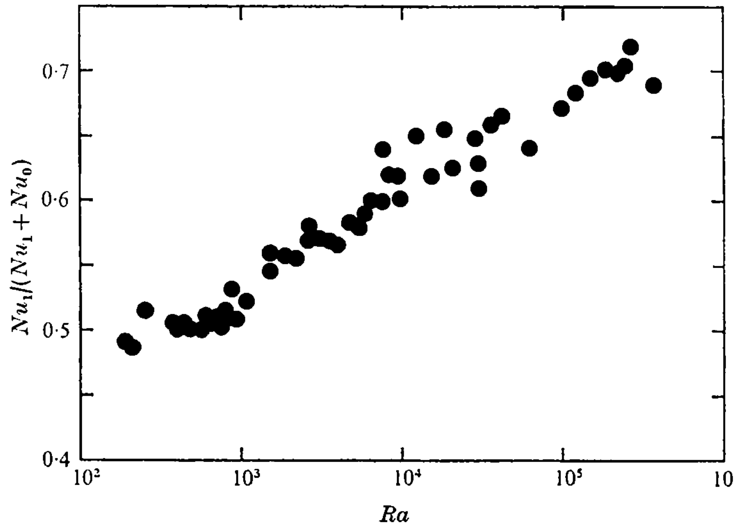

FIGURE 3. Fraction of energy transport at the upper boundary.

and at the lower boundary,

$$Nu_0 = (2{\cdot}006 \pm 0{\cdot}010)Ra^{0{\cdot}10}, \quad 580 \leqslant Ra \leqslant 3{\cdot}78 \times 10^5, \quad 5{\cdot}76 \leqslant Pr \leqslant 6{\cdot}35,$$

$$0{\cdot}05 \leqslant (L/X) \leqslant 0{\cdot}25, \quad r = 0{\cdot}974 \quad \text{from 67 observations.}$$

Additional correlations of the data are given in the appendix.

The measured energy transport at the system boundaries was, on the average, consistent with the fraction of power input associated with the volume of the fluid contained between the copper plates. It was assumed that the energy production in the fluid next to the electrodes (each being displaced 1·27 cm from the edges of the copper plates) did not affect the convective transport in the centre of the layer. An energy balance for the system was defined as BF = (total heat transport measured at the horizontal boundaries)/(electrical energy input between the copper plates). A check on experimental consistency from run to run (e.g. when the layer depth was increased) and on the internal consistency with a given run was thus possible. For low Ra (small layer depths) $BF \approx 1$; but for $Ra > 7 \times 10^3$, BF sometimes exceeded one. (Values of BF are given in table 1.) This indicated that advection was perhaps significant at larger plate separations. The overall one-dimensionality of the transport process could thus be questioned at the higher Ra. The correlations for energy transport presented here, however, include all the data regardless of the BF value associated with a given experiment. The Nu associated with the values of $BF \neq 1$ did not deviate significantly from either the overall trend in the energy transport or the computed correlations of Nu with Ra for either boundary, equations (6) and (7).

The possibility that discrete transitions might exist in the energy transport at the boundaries was investigated in view of the occurrence of such transitions for thermal convection with heating from below (Malkus 1954; Willis & Deardorff

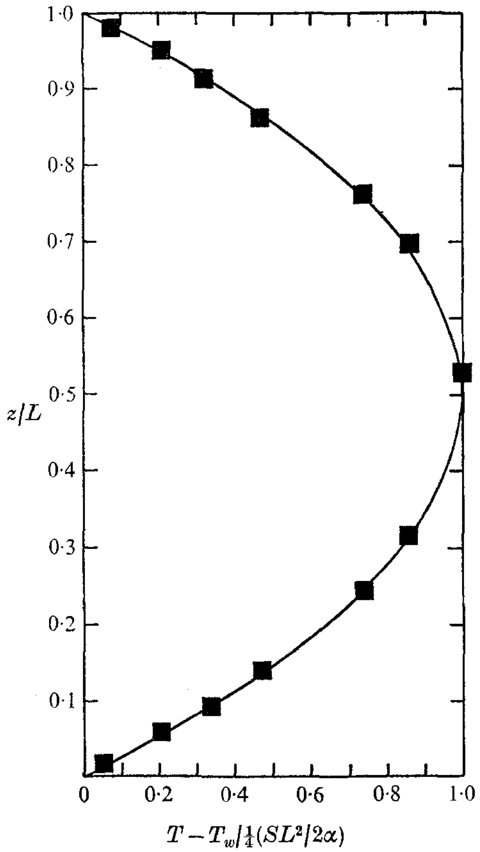

FIGURE 9. Dimensionless mean temperature distribution for conduction. Ra = 391·1, L = 1·27 cm, $\frac{1}{4}SL^2/2\alpha$ = 0·072 °C. ——, theoretical conduction profile.

1967; Krishnamurti 1970). A linear plot of $Nu.Ra$ versus Ra did reveal the existence of linear segments in the energy transport. However, transition values of Ra could not be defined with great precision. Furthermore, the apparent linear segments in the respective plots for the upper and lower boundaries were not strictly delimited by the same transition Ra. At the upper boundary, transition Ra were estimated to be 12 000, 92 000 and 195 000. For the lower boundary transition Ra were observed at 20 000 and 190 000. Transition points at lower Ra were not discernable with the present data.

5. Mean temperature profiles

Wedge fringe interferograms formed the basis of the energy transport measurements and are shown in figures 4–8 (plates 1–4) for selected values of Ra. Several spatially averaged temperature distributions (averaged both in the direction of the light beam and across the light beam over the central 5 cm of the layer) are presented in figures 9 and 10 for selected values of Ra covering the range of the data. The reduced temperature distribution near the upper boundary plotted

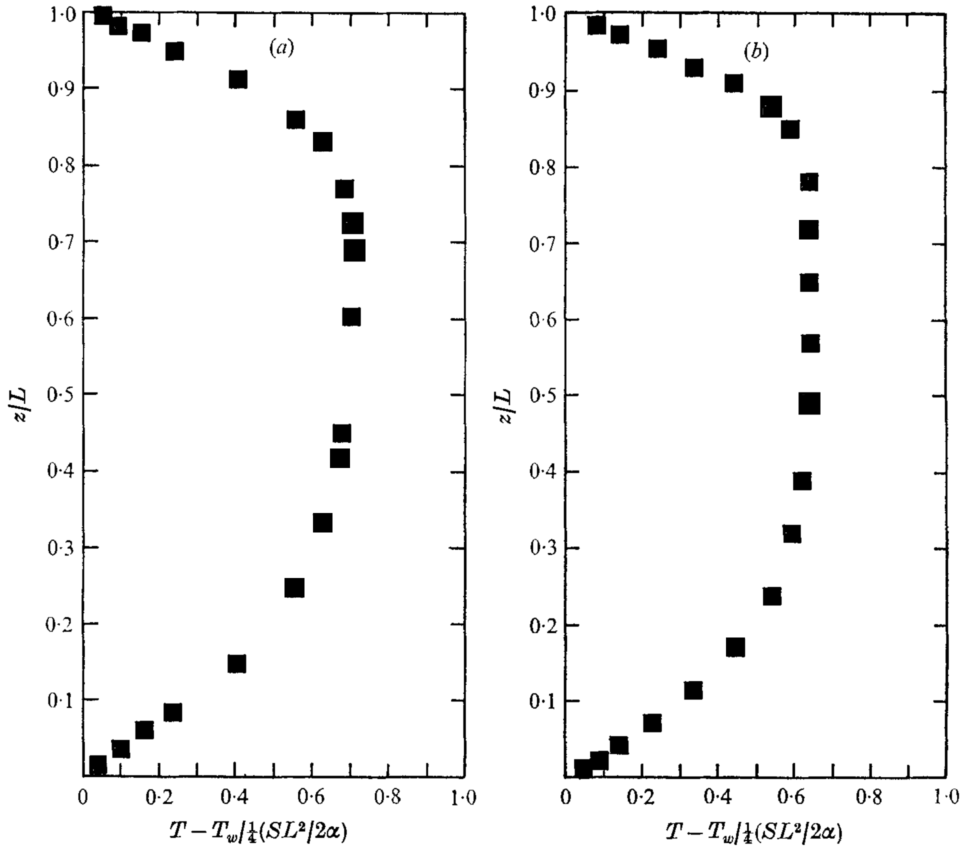

FIGURE 10 (*a*, *b*). For legend see facing page.

as a function of the thermal boundary-layer thickness δ (defined as $\delta = L/Nu$) is shown in figure 11. The solid curve in figure 11 is the least-squares curve for similarly reduced temperature data near the lower boundary.

A number of distinct features of low and high *Ra* convection were identified from the fringe field. In general, overall buoyant forces acting on the warm central core of the layer displace this region upwards, above the geometric centre of the layer (figure 13, plate 7). For $Ra \geqslant 2642$ the asymmetric nature of the mean temperature distribution appears fully developed and this asymmetry becomes more pronounced as *Ra* is increased. A quasi-periodic motion, viewed as a horizontal average in the direction of the light beam, dominates the regime $Ra < 10^4$. Separations between individual isothermal regions (enclosed by a single fringe as in figure 13) are apparently downdraft sites for cold flows from the upper boundary or upflow channels for entrained warm fluid from the central regions of the layer. (Updrafts in the sense of plume-type flows from the cooled lower boundary are prohibited by the positive mean temperature gradients in the lower portion of the layer.) A motion-picture study shows that variations in the spacing between wedge fringes for $Ra \approx 5000$ correspond to separations between individual isothermal regions. They are more or less periodic (as are the individual isothermal regions) across the field of view but are not stationary.

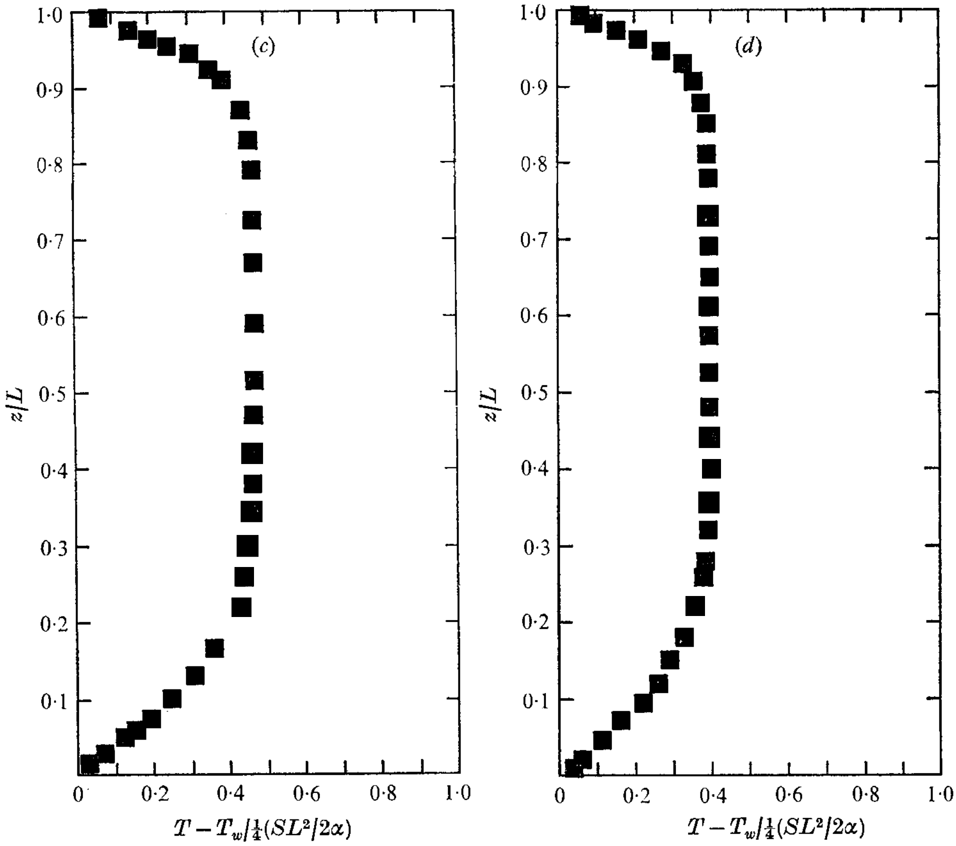

FIGURE 10. Dimensionless mean temperature distribution for natural convection. (*a*) $Ra = 5469$, $L = 2{\cdot}539$ cm, $\frac{1}{4}SL^2/2\alpha = 0{\cdot}122$ °C. (*b*) $Ra = 1{\cdot}582 \times 10^4$, $L = 3{\cdot}176$ cm, $\frac{1}{4}SL^2/2\alpha = 0{\cdot}193$ °C. (*c*) $Ra = 6{\cdot}320 \times 10^4$, $L = 5{\cdot}079$ cm, $\frac{1}{4}SL^2/2\alpha = 0{\cdot}173$ °C. (*d*) $Ra = 2{\cdot}738 \times 10^5$, $L = 5{\cdot}079$ cm, $\frac{1}{4}SL^2/2\alpha = 0{\cdot}549$ °C.

For $Ra > 10^4$, turbulent mixing effects begin to play the dominant role in the overall energy transport process, and any periodicity or near periodicity in the mean temperature fields evident at lower Ra begins to disappear. Turbulent convection is characterized by a well-mixed isothermal core (figure 10(*d*)) and the downward release of cold thermals from the edge of the thermal boundary layer at the upper surface. Figures 12 (*a*), (*b*) and (*c*) (plates 5 and 6) show the release of a thermal from the upper boundary at $Ra = 1{\cdot}27 \times 10^3$. The release of thermals from the upper boundary is a random process and appears in wedge fringe interferograms as randomly occurring waves travelling downward along one or several fringes. This is shown in figure 8 (plate 4) by the deformation of the fringes near the centre of the layer. Motion pictures of the turbulence reveal that downward-travelling thermals are sometimes able to maintain their 'thermal identity' until they reach the boundary layer at the lower surface.

Summarizing the observation of mean temperature fields it is possible to postulate the following approximate regimes of motion: (*a*) gentle laminar convection for $Ra_c \leqslant Ra \leqslant 5 \times 10^3$, where conduction is still a relatively important

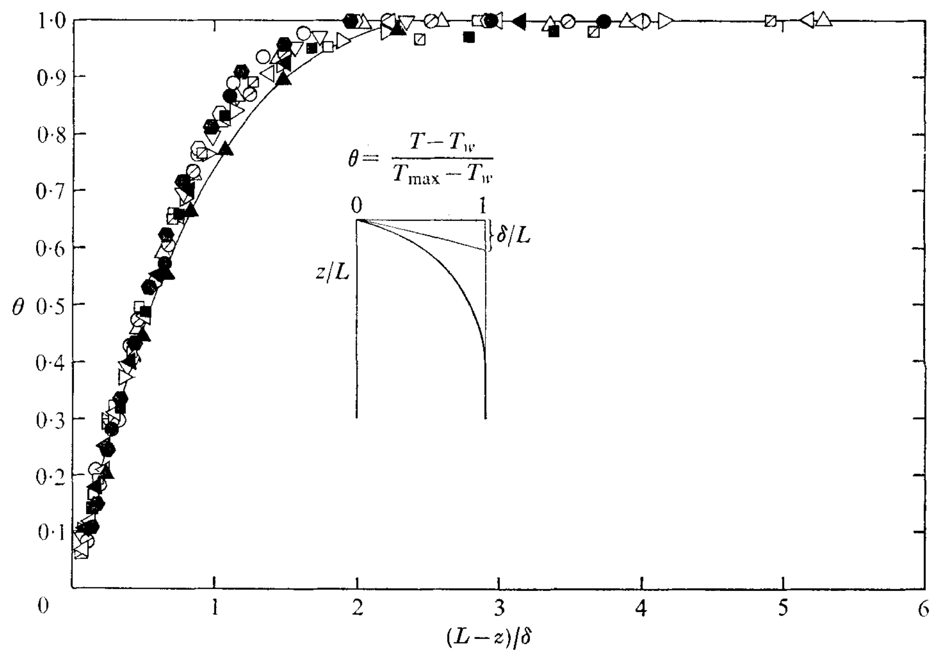

FIGURE 11. Reduced mean temperature near the upper boundary for turbulent convection.

	◁	⬢	⊘	▨	○	□	△
$Ra \times 10^{-4}$	2·909	3·098	3·632	4·199	6·320	10·25	12·72
	○	▽	■	▷	◀	●	▲
$Ra \times 10^{-4}$	14·98	16·78	20·19	22·23	24·87	27·38	37·85

mechanism for energy transport throughout the entire layer, (*b*) developed laminar convection for $5 \times 10^3 \leqslant Ra \leqslant 10^4$ and (*c*) transition to turbulent convection for $Ra > 10^5$.

6. Laminar convection and stability observations

In figure 13 (plate 7), time-sequence interferograms are presented for developed convection with the infinite fringe setting of the interferometer. Though it was found difficult to maintain the original truly infinite fringe adjustment throughout the period of each of the experiments (about three-quarters of a fringe net difference existed across the layer and produced fringes not exactly parallel to the layer boundaries), the interferograms are nevertheless qualitatively accurate visualizations of the thermo-fluid dynamic process within the layer.

Time-sequence interferograms at several *Ra* and motion pictures of laminar convection with the infinite fringe adjustment suggests a process of growth, coalescence and breakup of individual isothermal regions as a spatially and temporally irregular succession of events. In general, isothermal regions of large horizonal extent tend to absorb regions of smaller horizontal extent. If, however, an individual isothermal region becomes too large in horizontal extent, it

Ra	Pr	Ra/Ra_c ($Ra_c = 560$)	L (cm)	z_c/L	$\bar{d}_{cz}$	$\bar{d}_{cL,\,\mathrm{max}}$	$\bar{d}_{cL}$
1590	5.96	2·84	1·429	0·60	0·335	0·60–2·0	1·1
2995	5·96	5·35	1·429	0·66	0·244	0·40–1·4	0·8
5390	5·94	9·63	1·429	0·70	0·210	0·20–1·6	0·6

TABLE 2. Approximate dimensions and location relative to layer depth of regions of constant temperature in laminar convection with the infinite fringe adjustment of the interferometer.

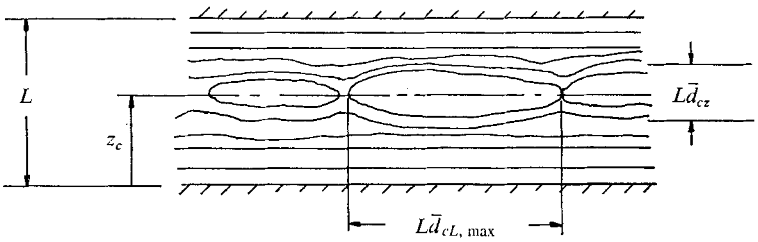

FIGURE 14. Sketch of notation used in table 2.

becomes unstable to flow disturbances (probably with the development of cold downflows) near the upper boundary and breaks apart to form a number of smaller isothermal regions. The breakup process begins as a local necking-down of the isothermal region as if it were being pulled in opposite horizontal directions at each end. The overall pattern of the isothermal regions in the centre of the layer is indicative of a cellular flow. Motion pictures reveal that these regions are neither truly periodic nor stationary. Once an isothermal region appears in the layer, it grows in both vertical and horizontal extent, the growth rate being roughly proportional to Ra. The vertical extent is limited to a fraction of the layer depth, which decreases as Ra increases. The horizontal extent varies about a mean value which also decreases with increasing Ra. Quantitative information on these features of the flow for three Ra values is presented in table 2 (see figure 14 for notation). These data were derived from discrete measurements using a limited number of interferograms for each Ra.

The correlation of the upper boundary Nusselt number, see (6), was chosen to estimate Ra_c. The lower boundary Nusselt number correlation was not used since some measured Nu_0 values for $Ra < 1000$ drop below 4·0 and because a slight change in the Ra exponent in the correlation could produce large changes in the estimated Ra_c. By extrapolating (6) to the theoretical pure conduction value $Nu_1 = 4{\cdot}0$, a critical Ra of 620 ± 30 was obtained.

For a comparison of existing theoretical predictions of Ra_c (Kulacki 1971) with the above-measured value, it is necessary to take into account the thermal coupling between the layer and its environment. This coupling is expressed theoretically by the Biot number Bi. For the convection chamber an equivalent Biot number Bi^{+} is defined as the ratio of the thermal conductance of the bounding wall to that of the fluid layer: $Bi^{+} = (k_w/L_w)/(k_f/L)$, where the conductance of the wall is obtained from the additive thermal resistance concept for a composite wall. The terms k_w, L_w, and k_f are, respectively, the effective thermal conductivity of the wall, the total thickness of the layer boundary, and the thermal conductivity of the fluid. Using nominal values from the literature for the material properties of the layer boundaries, we find that $Bi^+ = 47{\cdot}5(1 \pm 0{\cdot}15)$. At this value of Bi and for symmetrical thermal boundary conditions, the linear theory stability limit is $Ra_c = 560$ while the energy theory limit is $\widetilde{Ra}_c = 292$ (Kulacki 1971).

The possibility of convection at $Ra < 560$ was investigated qualitatively by introducing large-size random disturbances into the layer at $Ra = 485$. A glass rod was inserted into the layer at one edge of the system: stirring with large back-and-forth motions was then performed for periods of several minutes. During the stirring, the maximum temperature in the layer was reduced to approximately one-third of its value before stirring. The temperature distribution (i.e. wedge fringe field) returned to its original form about ten to fifteen minutes after stirring stopped. A comparison of interferograms before and after stirring showed no measurable difference between the maximum temperatures (maximum fringe shifts) in the layer and temperature gradients (fringe slopes) at the layer boundaries.

7. Error estimates

Systematic errors in wall temperature gradients arising from refraction of the light rays in the cooled boundary layers on the upper and lower copper plates were corrected with formulae which take into account the optical averaging property of the interferometer (Goldstein 1968, Kulacki 1971). The combined uncertainties in the thermophysical properties, geometrical factors and wattmeter readings produced an experimental uncertainty of 2–3 % in Ra. The temperature variation of the electrical conductivity of the electrolyte was neglected since the concentration of silver nitrate was low (0·02 molar) and maximum temperature differences in the fluid were of the order of 0·5 °C or less. Thus the total power consumed in the convection cell was taken directly from the wattmeter readings. The total experimental uncertainty in the computed values of Nu ranged from $\pm 3{\cdot}2\,\%$ to $\pm 6{\cdot}5\,\%$.

The research reported here was supported by National Science Foundation Grants GK 1737 and GK 15252. The award of a NSF Traineeship to F.A. Kulacki is appreciated.

Appendix

Additional correlations for the energy transport were computed over a reduced range of Ra for which the trends in the energy transport at each of the boundaries were clearly established. In the form of (5), the results were

$$Nu_1 = 0{\cdot}959 Ra^{0{\cdot}228 \pm 0{\cdot}004}, \quad 1104 \leqslant Ra \leqslant 3{\cdot}78 \times 10^5, \quad 0{\cdot}075 \leqslant (L/X) \leqslant 0{\cdot}25,$$
$$5{\cdot}76 \leqslant Pr \leqslant 6{\cdot}09, \quad r = 0{\cdot}991 \quad \text{from} \quad 47 \text{ observations}$$

and

$$Nu_0 = 2{\cdot}089Ra^{0{\cdot}095\pm0{\cdot}004}, \quad 1104 \leqslant Ra \leqslant 3{\cdot}78\times10^5, \quad 0{\cdot}075 \leqslant (L/X) \leqslant 0{\cdot}25,$$
$$5{\cdot}76 \leqslant Pr \leqslant 6{\cdot}09, \quad r = 0{\cdot}963 \quad \text{from 47 observations.}$$

A correlation of the form

$$(Nu-4) = C(Ra-Ra_c)^m$$

was also computed for all measured Nu greater than the theoretical pure conduction value of 4·0. For the upper boundary

$$(Nu_1-4) = 0{\cdot}037(Ra-560)^{0{\cdot}489\pm0{\cdot}028}, \quad 703 \leqslant Ra \leqslant 3{\cdot}78\times10^5,$$
$$0{\cdot}062 \leqslant (L/X) \leqslant 0{\cdot}25, \quad 5{\cdot}76 \leqslant Pr \leqslant 6{\cdot}35, \quad r = 0{\cdot}934 \text{ from 48 observations}$$

and at the lower boundary

$$(Nu_0-4) = 0{\cdot}0097(Ra-560)^{0{\cdot}483\pm0{\cdot}003}, \quad 703 \leqslant Ra \leqslant 3{\cdot}78\times10^5,$$
$$0{\cdot}062 \leqslant (L/X) \leqslant 0{\cdot}25, \quad 5{\cdot}76 \leqslant Pr \leqslant 6{\cdot}35, \quad r = 0{\cdot}919 \quad \text{from} \quad \text{48 observations.}$$

No significant reduction in the error sum of squares of the regression of Nu on Ra could be achieved by including the Prandtl number or layer aspect ratio.

REFERENCES

Bethe, H. A. 1968 *Science*, **161**, 451.

French, K. W. 1968 MS thesis, University of Minnesota.

Goldstein, R. J. 1968 Optical Measurements of temperature. *Heat Transfer Lab. Rep. Mech. Eng. Dept., University of Minnesota*: HTL 86. (See also Eckert, E. R. G. & Goldstein, R. J. (eds.) 1970 Measurement techniques in heat transfer. *AGARDograph*, no. 130 (with errata), pp. 177–228.)

Knopoff, L. 1967 *The Earth's Mantle* (ed. T. F. Gaskell), chap. 8. Academic.

Krishnamurti, R. 1970 *J. Fluid Mech.* **42**, 2, 295.

Kulacki, F. A. 1971 Ph.D. thesis, University of Minnesota.

Malkus, W. V. R. 1954 *Proc. Roy. Soc.* A **255**, 185.

Novotny, J. L. 1963 Ph.D. thesis, University of Minnesota.

Runcorn, S. K. 1962 *Nature*, **195**, 1248.

Schwiderski, E. W. & Schwab, H. J. A. 1971 *J. Fluid Mech.* **48**, 703.

Tozer, D. C. 1966 *Proc. Roy. Soc.* A **258**, 252.

Tritton, D. J. & Zarraga, M. N. 1967 *J. Fluid Mech.* **30**, 21.

Wilkie, D. & Fisher, S. A. 1963 *Proc. Instn. Mech. Engrs.* **178**, 461.

Willis, G. E. & Deardorff, J. W. 1967 *Phys. Fluids*, **10**, 1861.

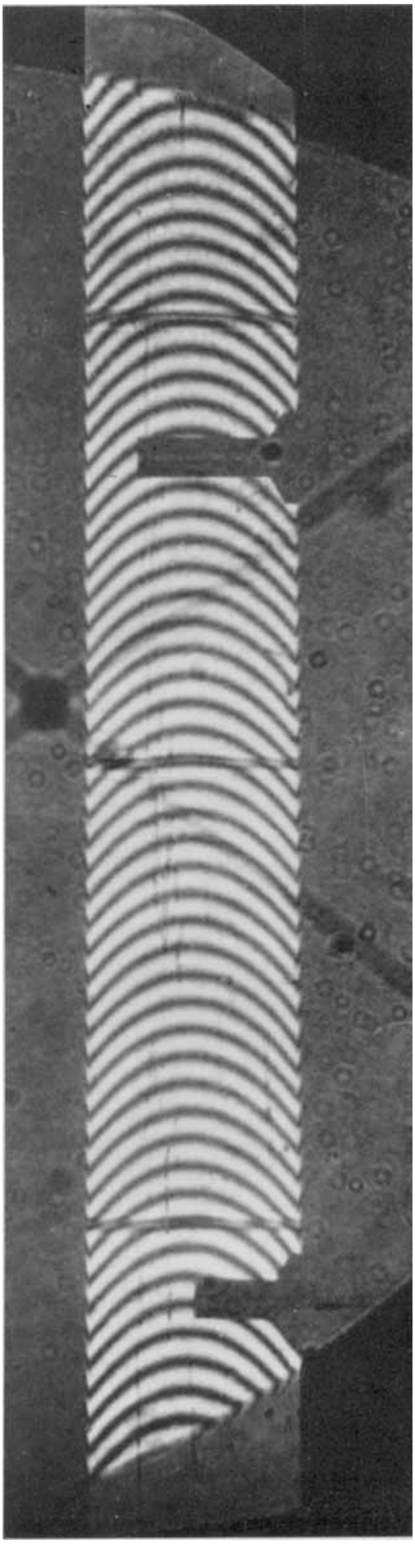

FIGURE 4. Interferogram of conduction state. $Ra = 258\cdot9$, $L = 1\cdot27$ cm.

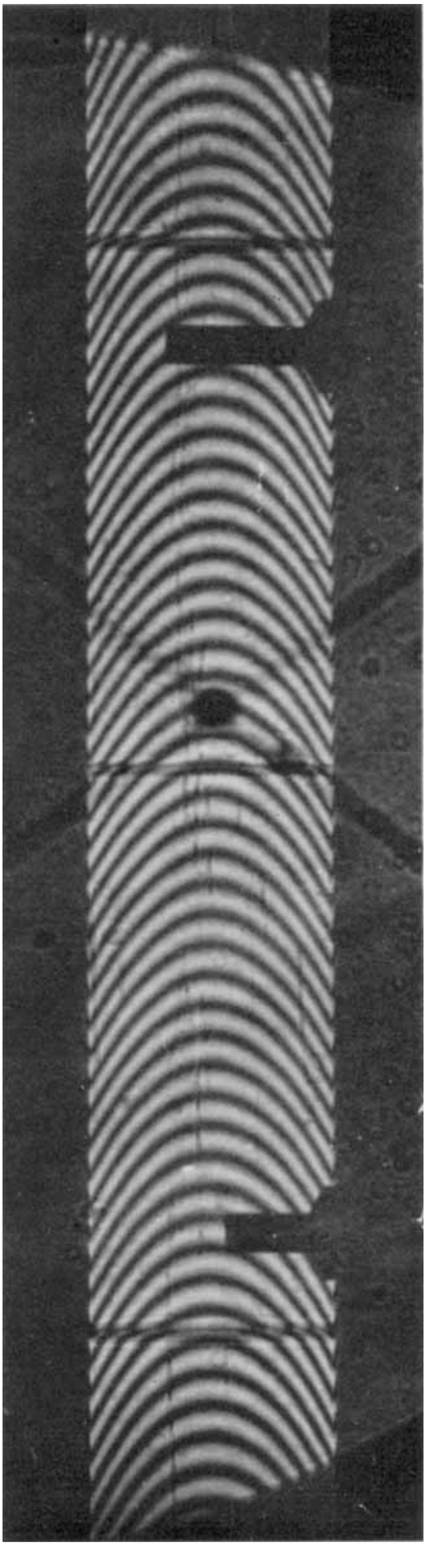

FIGURE 5. Interferogram of natural convection. $Ra = 580\cdot5$, $L = 1\cdot429$ cm.

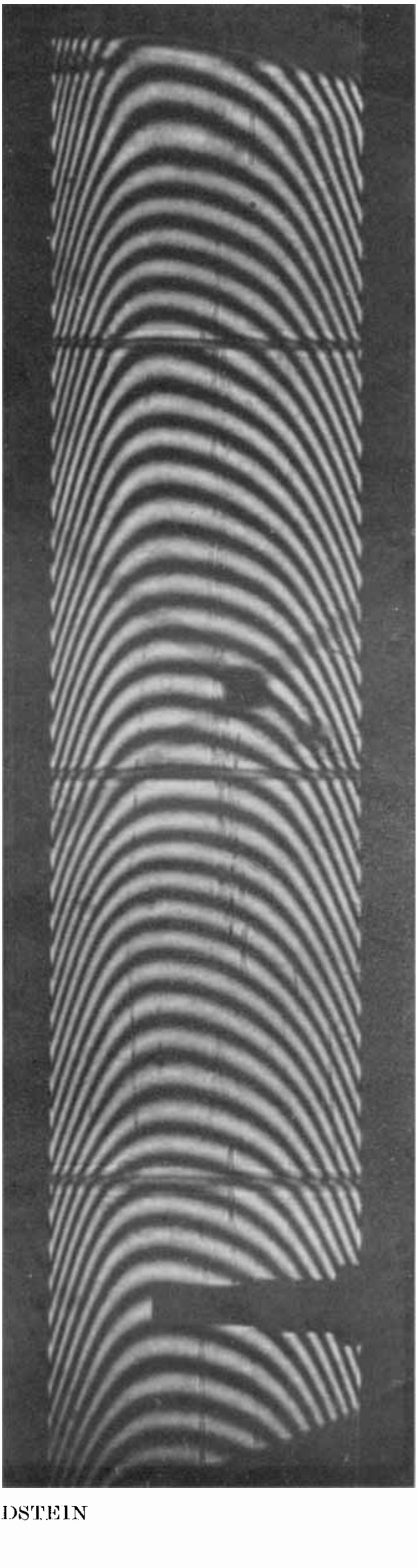

Figure 6. Interferogram of natural convection. $Ra = 2642$, $L = 1{\cdot}906$ cm.

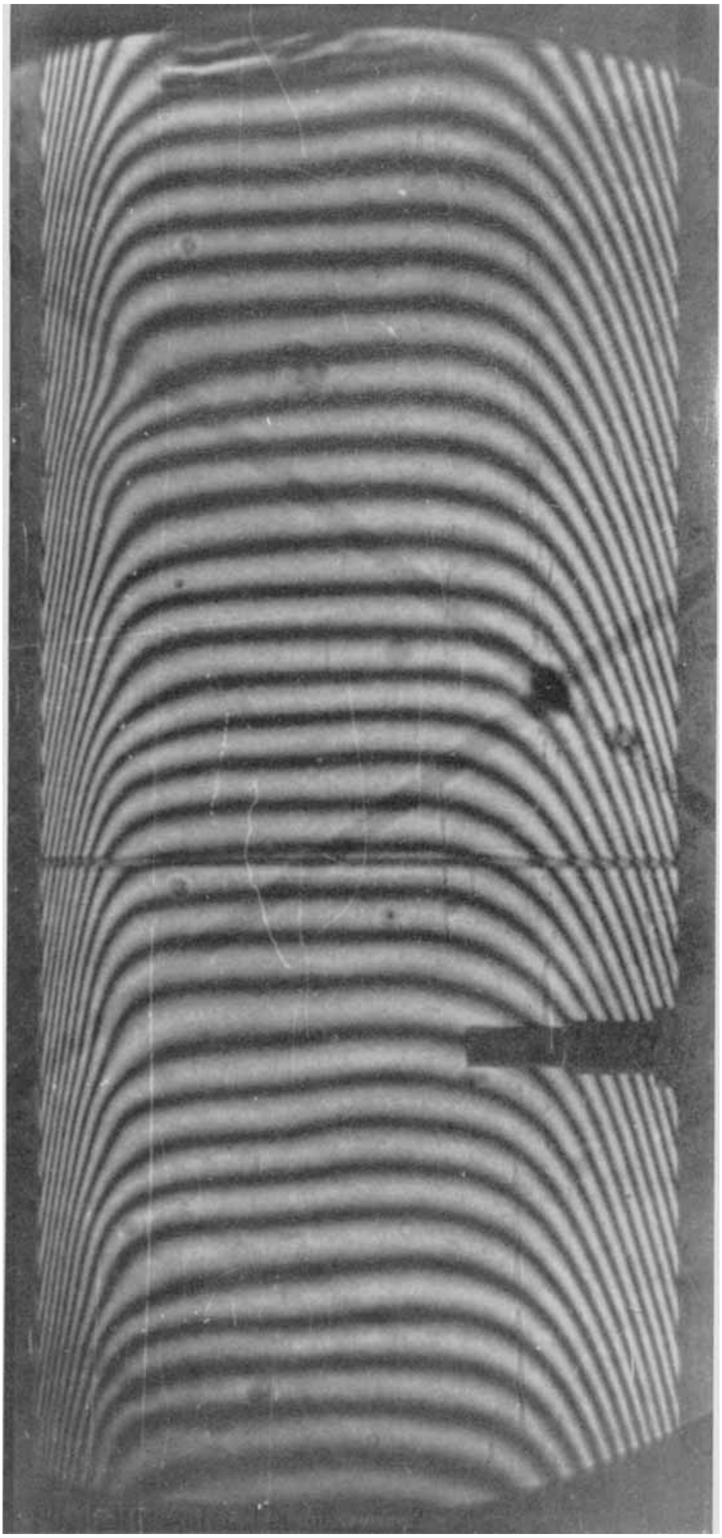

FIGURE 7. Interferogram of natural convection. $Ra = 4{\cdot}199 \times 10^4$, $L = 3{\cdot}809$ cm.

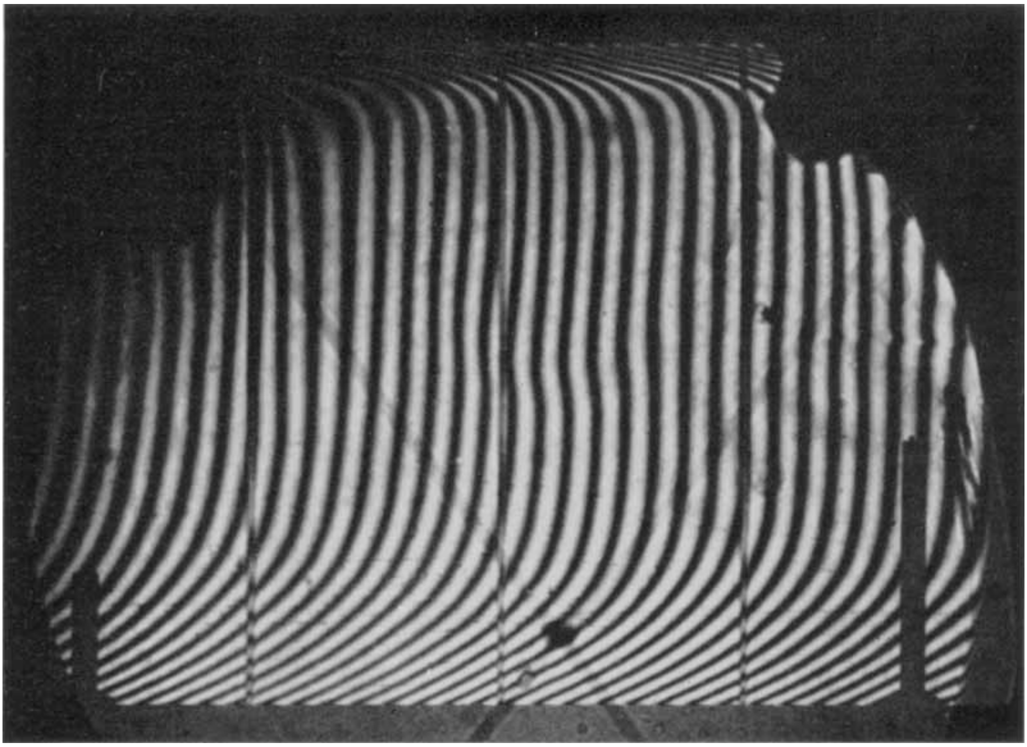

FIGURE 8. Interferogram of natural convection. $Ra = 2{\cdot}738 \times 10^5$, $L = 6{\cdot}352$ cm.

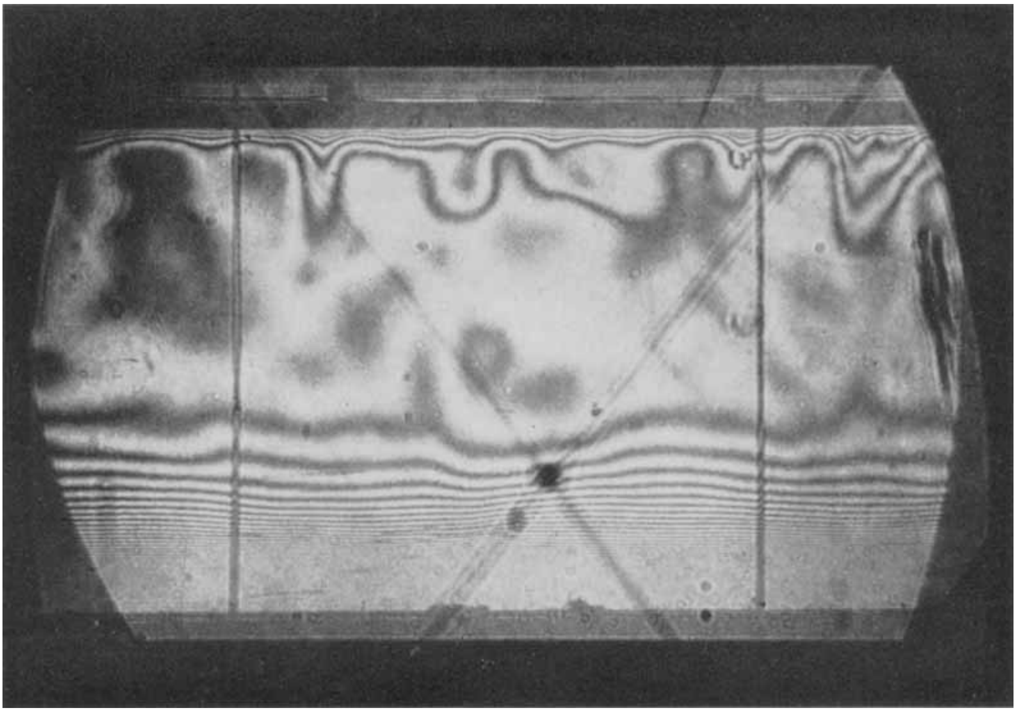

(*a*)

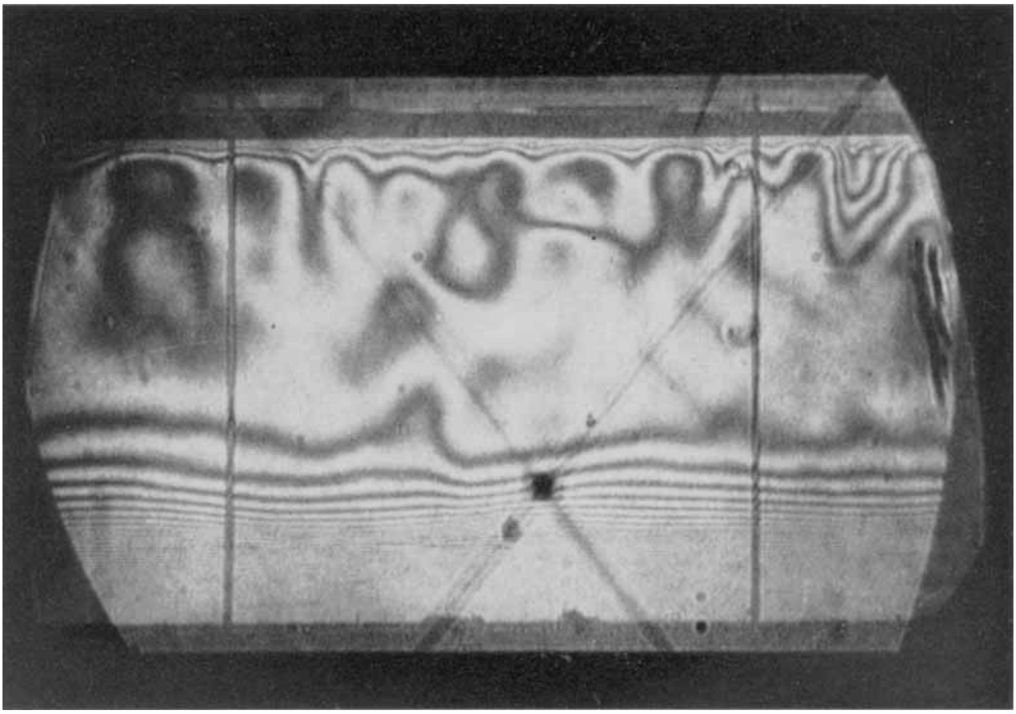

(*b*)

FIGURE 12 (*a*, *b*). For legend see plate 6.

[redacted]

[redacted]

(*c*)

FIGURE 12. Interferograms of turbulent convection with infinite fringe adjustment. Interferograms are one second exposures five seconds apart. $Ra = 1{\cdot}27 \times 10^6$, $L = 5{\cdot}08$ cm. The upper boundary is obscured owing to refraction effects.

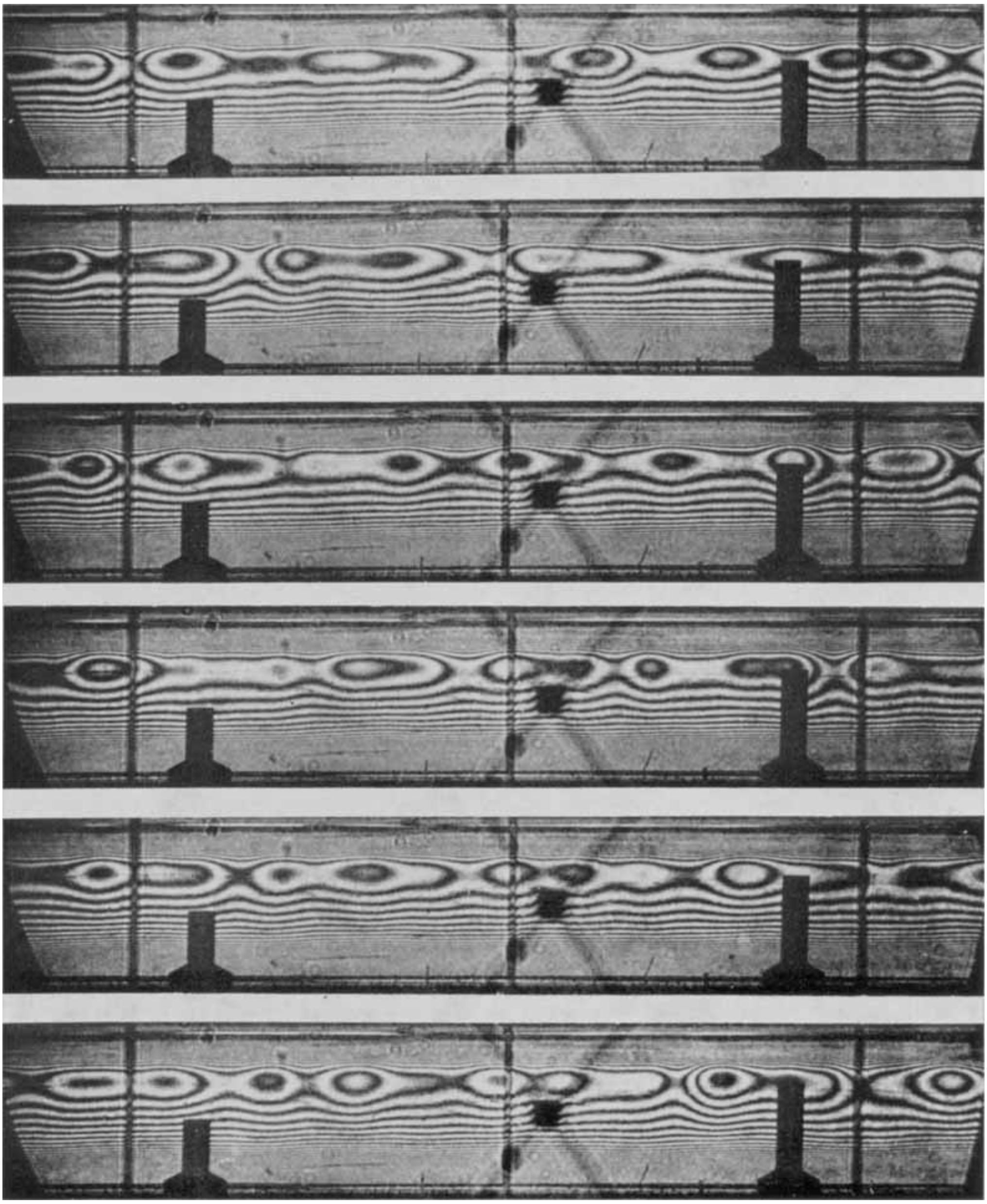

FIGURE 13. Time-sequence interferograms at 60 s intervals with infinite fringe adjustment. $Ra = 5390$.